Materials Science and Engineering B 301 (2024) 117200

Contents lists available at ScienceDirect

Materials Science & Engineering B

journal homepage: www.elsevier.com/locate/mseb

Effect of rare earth Europium (Eu^{3+}) on structural, morphological, magnetic and dielectric properties of $NiFe_2O_4$ nanoferrites

P. Sivaprakash [a,1], S. Divya [b,1], S. Esakki Muthu [c], Amanat Ali [d], Zvonko Jaglicic [e], Tae Hwan Oh [b,*], Ikhyun Kim [a,*]

[a] Department of Mechanical Engineering, Keimyung University, Daegu 42601, Republic of Korea
[b] School of Chemical Engineering, Yeungnam University, Gyeongsan 712-749, Republic of Korea
[c] Centre for Material Science, Department of Physics, Karpagam Academy of Higher Education, Coimbatore 641 021, India
[d] College of New materials and Nanotechnologies, National University of Science and Technology MISIS, Moscow, Russia
[e] Faculty of Civil and Geodetic Engineering, University of Ljubljana, Jamova 2, SI-1000 Ljubljana, Slovenia Institute of Mathematics, Physics and Mechanics, Jadranska 19, SI-1000 Ljubljana, Slovenia

ARTICLE INFO

Keywords:
Nanoparticles
Transition metal ions
Spinel ferrite
Rare earth
Europium doped Nickel ferrite
Dielectric and magnetic properties

ABSTRACT

Herein, rare earth Eu^{3+}-doped $NiFe_2O_4$ (x = 0.00, 0.04, 0.08, 0.12) nanoferrites are prepared using the sol–gel auto combustion method. The effect of Eu^{3+} doped $NiFe_2O_4$ on the structural, morphological, thermal, magnetic, and dielectric properties of $NiFe_2O_4$ is observed. XRD patterns of samples confirm that samples x = 0.00, 0.04, and 0.08 possess a single-phase FCC structure with a space group of Fd3m, whereas the sample x = 0.12 exhibits secondary phase $EuFeO_3$ formation at higher Eu^{3+} concentrations. The lattice constant (a_c) and cell volume increase with increasing Eu content based on XRD analysis. Furthermore, TGA analysis reveals thermal decomposition and weight loss in pure and doped materials. According to the FESEM analysis, the addition of Eu^{3+} results in nanoparticles (NPs) with an average grain size of 220–250 nm, and the EDAX spectrum indicates the presence of Eu, Ni, Fe, and O, as confirmed through elemental mapping. Additionally, room-temperature magnetic hysteresis curves show clearly defined soft FM behavior for all prepared NPs, with saturation magnetization (M_s) values in the range of 48.42——43.15 emu/g and remnant magnetization (M_r) in the range of 32.64——23.65 emu/g. However, the overall coercivity increases (90——140 Oe) by substituting Eu^{3+} ions at the Fe^{3+} site. Furthermore, all the samples' dielectric constants (ε') are high at low frequencies and gradually decrease as the frequency increases, there by confirming Koop's theory. Moreover, owing to the decreased hopping rate for Fe^{3+} at the octahedral sites in the doped NPs, the dielectric constant (ε') and loss factor (tan δ) both decrease with the substitution of Eu^{3+}. Hence, the lower tan δ values indicate that Eu^{3+}-doped $NiFe_2O_4$ NPs are appropriate for high-frequency microwave device applications.

1. Introduction

Spinel ferrites (MFe_2O_4, where 'M' is any divalent metal ion) have long been the focus of research because of their technological and scientific applications in the fields of electronic devices, magnetic materials, and optical devices, as well as in electrochemical science and technology, ferrofluids, synthetic biology, and high-frequency storage systems [1,2]. Additionally, the potential use of MFe_2O_4 compounds as electrode materials in Li-ion batteries and solid oxide fuel cells has recently received considerable attention [3–5]. These materials exhibit unique properties, such as large DC electrical resistivity, large saturation magnetization, and high permeability at high frequencies, which are ideal for application in magnetic materials and electronic devices [6,7]. The structural formula of these ferrites is MFe_2O_4, where M is a divalent metal ion derived from Mn^{2+}, Fe^{2+}, Co^{2+}, Ni^{2+}, Cu^{2+}, Zn^{2+} or the composition of these elements. Other ions that can be incorporated into the spinel lattice include Li^{+}, Mg^{2+}, Cr^{3+}, Ti^{4+}, and Sb^{5+}. These metal ions have also been widely used as transformer cores in electronic applications owing to their high resistivity and soft FM nature [7]. According to the composition, the spinel structure of the MFe_2O_4 family typically has a lattice parameter (a_c) of 8.30–8.50 Å. Additionally, the unit cell can incorporate metal ions into 64 possible tetrahedral (or A)

* Corresponding authors.
E-mail addresses: taehwanoh@ynu.ac.kr (T. Hwan Oh), kimih@kmu.ac.kr (I. Kim).
[1] Authors are equally contributed.

https://doi.org/10.1016/j.mseb.2024.117200
Received 30 June 2023; Received in revised form 6 November 2023; Accepted 24 November 2023
Available online 20 January 2024

and 32 possible octahedral (or B) interstices or sites [8]. Here, metal cations were present at only 8B and 16 A sites. Because of magnetic interactions, two nearby magnetic ions on the B-site are connected in a parallel manner (ferromagnet (FM)), as compared with the much larger antiparallel (antiferromagnet (AFM)) coupling between the magnetic ion on the A-site and the ions at the B-sites. Ferrimagnetism (FI), the net magnetic moment (μ_B) in a magnetic material with dominant magnetic interaction in AFM, results from two ions antiparallel coupled to each magnetic ion on the A site [9,10].

Among the ferrite family, centrosymmetric magnetic nanophase $NiFe_2O_4$ (NFO) is a well-known material that has received considerable attention owing to its unique inverse spinel structure, soft FM nature, and electric properties. The ductility and hardness of transition metal oxide mixed with ferrite materials render it useful in aerospace technology, and it has a wide range of technically outstanding potential applications in electronic devices, magnetic fluids, organic synthesis, microwave adsorbents, smart tape and disc recordings, magnetic refrigerators, magnetic levitation system, magnetic drug delivery, and magnetic fluids. [10,11]. Ferrite has an FCC structure, in which Fe^{3+} ions are equally distributed between the A and B positions, whereas Ni^{2+} ions occupy only the B site, with the spinel structure corresponding predominantly to the Fd-3 m space group. Additionally, it has a high Curie temperature, T_C, of approximately 558 °C, modest saturation magnetization value, M_S, (approximately 56 emu.g^{-1}), high permeability (1.26–7.54 10^4H/m), high electrical resistivity (7×10^8 Ω. m), and low loss factor (>1) [12–14]. However, the preparation technique, particle size and surface morphology, processing atmosphere, and cation substitution in the host material for Fe^{2+}/Fe^{3+} ions have a significant impact on the structural, dielectric, and magnetic properties of NFO [15,16]. In addition, incorporating suitable elements at the Ni/Fe site has been found to be beneficial for fine-tuning the magnetic and electrical properties, and the addition of rare earth elements (REE, such as La^{3+}, Sm^{3+}, Gd^{3+}, Dy^{3+}, Yb^{3+}, Er^{3+}, Tb^{3+}, and Ce^{3+}) consistently influences the nature [17–20].

In addition, numerous researchers have investigated how REE ion replacement affects the magnetic characteristics of ferrite materials, particularly in light of the use of these materials in magneto–optical (MO) storage, MO sensors, and hyperthermia therapy [21]. The addition of REE ions to Ni/Fe ferrite results in significant changes in the results, such as lattice distortion and structural disorder, thereby allowing the tuning of the electrical, magnetic, and dielectric properties of the material composition [22]. Consequently, the structural, magnetic, and dielectric properties are assumed to change significantly when a moderate amount of REE ions is substituted for Fe^{3+} ions. Here, to control the magnetic transition temperature between the superparamagnetic (SPM) and FM phases in nanoparticles (NPs), μ_B is methodically varied by the successive filling of electrons into 4f shells and the potent influence of spin–orbital (3d–4f) coupling, which all affect the structure and magnetic properties [23].

Numerous studies have been conducted to better understand the effects of REE doping on the physical, structural, morphological, and magnetic properties of ferrite materials. Given that REE ions have unpaired 4f electrons and strong spin–orbit coupling, adding them to the spinel ferrite crystal structure causes 3d–4f coupling, which can change the spectral, structural, magnetic, and electrical properties of MFe_2O_4 [23]. In accordance with these reports, Almessiere et al. reported the substitution of higher Dy^{3+} ionic radii at a lower Fe^{3+} ion radii site in NFO; this strengthened the super-exchange interaction between NPs and improved the magnetic properties, including remanence (M_r), coercivity (H_C), and μ_B [24]. Similarly, the author claimed that the substitution of Nb^{3+} at the Fe^{3+} site of $CoFe_2O_4$ (CFO) results in FM behavior at room temperature (RT), increases in M_S (44.45–49.40 emu. g^{-1}) and M_r (12.16–17.90), and decreases in H_C with Nb^{3+} [24,25]. Similarly, Zubair et al. reported enhanced magnetic properties through the substitution of Eu^{3+} ions using the co-precipitation method. This addition in CoFe2O4 led to ferrimagnetic behavior, variations in the anisotropy constant, and changes in coercivity [26]. Furthermore, the antibacterial activity of REE of Ce^{3+} in the ferrite material of CFO at the Co site is enhanced, and the magnetic properties of the material are altered [27]. S. Ravi Kumar et al. reported that the bi-metallic combination of $Co_{0.5}Ni_{0.5}Fe_2O_4$ material with Nd^{3+} at Fe^{3+} site improved the DC resistivity properties in addition to M_S [28]. Furthermore, Akhtar et al. reported graphene-based NFO (G/NFO) with REE's (Yb^{3+}, Gd^{3+}, and Sm^{3+}) dopants and G/NFO with REE's$^{(3+)}$ enhanced the M_S from 11.5 to 46.2 emu.g^{-1} for composite materials. Several studies have reported that replacing certain metal ions with rare-earth elements can improve their structural and magnetic properties [29]. The electromagnetic properties of MFe_2O_4 materials are affected by the types, sizes, and oxidation states of the ions, as well as how they are distributed between A and B sites.

In this study, Eu^{3+}- doped NFO, a nonmagnetic material with an iron vacancy at the Fe^{3+} site, is investigated. The addition of trivalent rare earth Eu^{3+} cations result in Fe^{3+}– REE^{3+} interactions, which may result in a change in the dielectric and magnetic characteristics. Herein, Eu^{3+} atoms are systematically introduced into the Fe^{2+} site, and materials are developed using the sol–gel auto combustion synthesis method to study the structural, morphological, dielectric, and magnetic properties of NFO. By characterizing these aspects, we aim to gain a detailed understanding of the way the introduction of Eu^{3+} ions influence the material magnetic properties, providing insights that can have implications for various applications.

2. Experimental procedure

2.1. Synthesis process

Analytical grade Nickel nitrate (Ni $(NO_3)_2{\cdot}6H_2O$), Iron nitrate (Fe $(NO_3)_3{\cdot}9H_2O$), and Europium nitrate (Eu $(NO_3)_2{\cdot}5H_2O$ with 99.99 % purity) chemicals were purchased from Sigma Aldrich. The sol–gel auto combustion method was used to prepare $NiEu_xFe_{2-x}O_4$, where $x = 0.00$, 0.04, 0.08, 0.12 NPs. Further, Ni $(NO_3)_2{\cdot}6H_2O$ and Fe $(NO_3)_3{\cdot}9H_2O$ were dissolved in deionized water in a ratio of 1:2 M and stirred separately for 20 min. Finally, the solution was gradually mixed with an aqueous solution of citric acid acted as a combustion agent ($C_6H_8O_7$) and heated to 80 °C while stirring. Following ignition, the ash product was heated to 100 °C to evaporate excess water. To form pure-phase crystals, the finished products were annealed for 2 h at 800 °C with a rate of 7 °C/min. The synthesized materials of $NiEu_xFe_{2-x}O_4$, where $x = 0.00$, 0.04, 0.08, 0.12 NPs referred to as Eu-0, Eu-4, Eu-8, and Eu-12, respectively.

2.2. Characterization Technique

Powder X-ray diffraction (XRD) was performed using a Rigaku Smart-Lab XRD instrument with Cu K radiation operating at 40 kV and 30 mA, and field emission scanning electron microscopy (FESEM, Zeiss Ultra 55) was employed for morphological analyses. Further, thermogravimetric analysis (SII TG/DTA 6200 EXSTAR) was performed in a nitrogen atmosphere from 25 to 1000 °C at a heating rate of 5 °C/min to study the stability and weight loss trends of the samples at these temperatures. Using a magnetic property measurement device (Quantum Design, MPMS 3), isothermal magnetization was measured at an applied magnetic field of 2.5 T, and the thermomagnetic properties were investigated at zero-field cooling and field cooling between 300 K and 2 K in the helium temperature range. To conduct the dielectric analysis, a programmable precision LCR bridge (Key sight: E4980A) was utilized in the frequency range ranging from 100 Hz to 2 MHz at RT, and a highly conductive layer of silver was placed on both sides of the pellet (13 mm × 1.2 mm) to enhance the ohmic contact of the materials.

3. Results and discussion

Fig. 1 shows the Rietveld refinement fit performed using the FULLPROF program to obtain the structural parameters of the Eu-doped

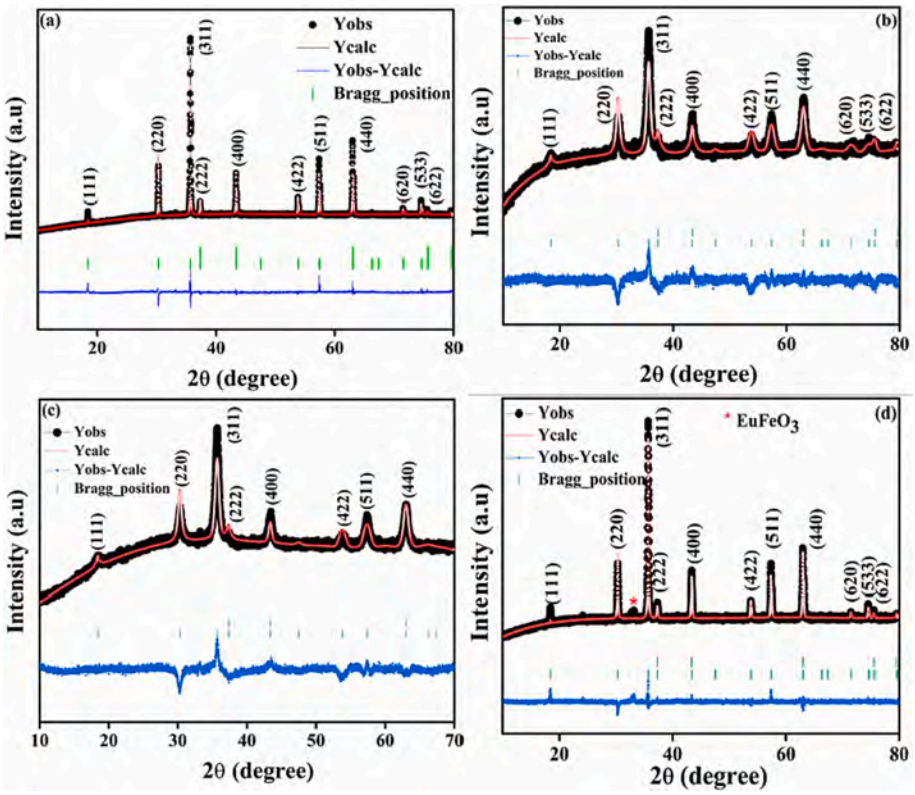

Fig. 1. Rietveld refinement fit of Eu-doped NFO NPs XRD patterns (a-d) Eu = 0—12.

$NiFe_2O_4$ NPs. The observed 2Θ values were 18.75°, 30.66°, 35.90°, 37.53°, 43.79°, 54.09°, 57.72°, and 63.43°, respectively, tus confirming the single-phase, FCC structure with a space group of Fd3m; they are in good agreement with the values on the reference JCPDS card no: 86–226 [9,10]. Evidently, with increasing Eu^{3+} substitution (Eu = 12) in pure spinel ferrite, the secondary phase of $EuFeO_3$ was observed at the maximum substitution of Eu, similar to the observations reported by Zubair et al. regarding the secondary phase of $EuFeO_3$ [26].

The secondary phase of $EuFeO_3$ is found at 2Θ = 33.3° with miler indices of (0 0 2) and is confirmed by the ICSD collection code of 189728. As the percentage of Eu^{3+} in the pure spinel lattice increases, the divergence from a single cubic phase becomes visible with the formation of secondary phase peaks containing a negligible amount of ortho ($EuFeO_3$) phase. The amount and type of dopant (Eu^{3+}) utilized determines the formation of secondary phases during the sintering technique. As a result, small amounts of Eu3 + ions added to the nickel ferrite lattice can affect both the size of the spinel matrix and the phase composition. Evidently, the ionic radius of Eu^{3+} had a significant impact in the formation of the $EuFeO_3$ phase in $NiFe_{2-x}Eu_xO_4$ samples. Eu^{3+} ions were greater (1.07) compared with the Fe^{3+} ions (0.67) [26,30]. Furthermore, the amount of Fe^{3+} ions that can be replaced by Eu^{3+} at the octahedral site of the spinel system. This implies that excess Eu^{3+} forms the Eu_2O_3 phase as an impurity on the grain boundaries. The high intensity peak of the reflection plane (3 1 1) shifted toward the low diffraction angle with increasing Eu content owing to the internal stress produced by the distribution of dopant cations [31]. The structural parameters of the pure and Eu^{3+} doped NFO sample were calculated using the following formulae [14].

$$D = k\lambda/(\beta \cos\theta), \quad (1)$$

$$a = d_{hkl}\sqrt{h^2 + k^2 + l^2}, \quad (2)$$

$$v = a^3, \quad (3)$$

$$\rho_x = \frac{8M}{Nv^3}, \quad (4)$$

$$L_A = \sqrt{3}\,\frac{a}{4}, \quad (5)$$

$$L_B = \sqrt{2}\,\frac{a}{4}, \quad (6)$$

where D represents the average crystallite size in nanometers; k represents the shape factor, with a value 0.94; β represents FWHM; λ denotes the wavelength of X-rays used; Θ is for the Bragg's diffraction angle; a_c is the lattice constant; d is the interplanar spacing; *h, k, and l* are the miller indices; *v* is volume of the unit cell; M is the molecular mass; and N is the Avogadro's number. The typical crystallite size of the samples was observed in the range of 29–33 nm. As the Eu content increased, the tensile strain increased. The presence of Eu^{3+} ions in the samples, which are larger in size compared with Fe^{3+} ions, was thought to increase the tensile strain with Eu concentration [32]. Eu^{3+} ions replaced the smaller Fe^{3+} ions, thereby leading to an increase in a_c from 8.26 to 8.30 Å and cell volume from 564.4 to 573.3 $Å^3$. Owing to the substitution of Eu^{3+} ions, the X-ray density increased from 5.42 to 5.46 g/cm^3. With higher Eu concentrations, the hopping length of A-sites and B-sites increased because the charge carriers required more energy to migrate between cationic site, thereby decreasing the conductivity [14]. The fitting parameters goodness-of-fit (χ^2), weighted profile reliability (R_{wp}), and profile reliability index (R_p) were used herein to analyze the refinement's accuracy (Table 1). The observed and calculated diffraction patterns were found to have a strong relationship, thus indicating that the goodness of fit (χ^2) was less than 10 %.

In the first phase, weight loss was attributed to the decomposition and oxidation of the sample contents at 500C. Here. the phase involved the crystallization of spinel ferrite. These peaks indicate the processes of crystallization and decomposition. The results of thermogravimetric examination at 5 °C/min in nitrogen to evaluate the thermal behavior

Table 1
The structural parameters of the Eu^{3+} doped $NiFe_2O_4$.

Eu^{3+}	D (nm)	a (Å)	V (Å^3)	ρ_x (g/cm^3)	L_A	L_B	$\chi 2$	R_{wp}	R_p
Eu-0	33.4	8.26	564.43	5.42	3.57	2.92	3.9	20.4	31.5
Eu-4	30.2	8.28	568.68	5.42	3.58	2.92	3.1	16.3	30.8
Eu-8	29.1	8.30	573.30	5.50	3.59	2.93	3.3	34.9	30.7
Eu-12	29.0	8.30	573.30	5.46	3.59	2.93	3.5	34.8	33.0

and stability of pure and Eu^{3+}-doped NFO NPs is shown in Fig. 2. The sample shown in Fig. 2(a) demonstrates that thermal decomposition occurred in two distinct steps. The initial 0.1 % weight loss step occurred between 25 and 400 °C and was associated with the elimination of hydroxyl groups [33]. The residual fuel caused the second weight loss step, which was 0.3 %, occurring between 400 and 800 °C. The last range of weight loss, at 800–1000 °C, resulted in the formation of crystalline $NiFe_2O_4$. A weight loss step of 0.1 % in the temperature range of 25–150 °C is shown in Fig. 2(b). The residual fuel caused the second weight loss step, which was 0.1 % and occurred between 250 °C and 800 °C. The last range of weight loss at 800–1000 °C temperature resulted in the formation of crystalline $NiFe_2O_4$. The sample in Fig. 2(c) displays weight loss steps of 0.1 % up to 600 °C, which corresponds to the removal of hydroxyl groups. The removal of leftover fuel caused a subsequent 0.3 % weight loss step, which was observed in the temperature range of 600–800 °C. The formation of crystalline $NiFe_2O_4$ was indicated by the final loss in the temperature range of 800–1000 °C [34].

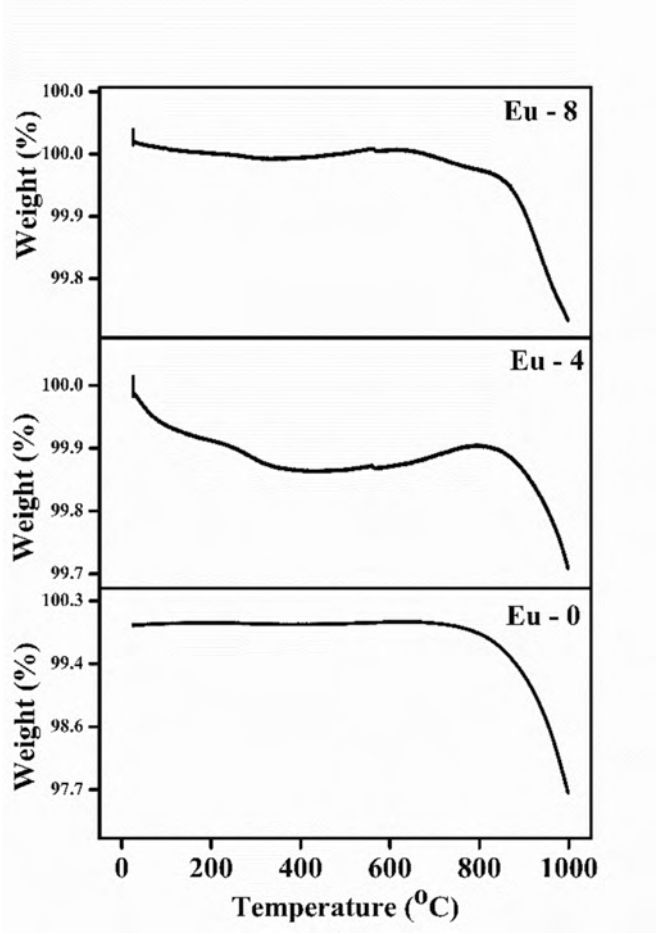

Fig. 2. TGA analysis of Eu-doped NFO NPs (a-c) Eu = 0, 8, and 12.

Samples of pure and Eu^{3+} doped NFO NPs are depicted in the FESEM micrographs in Fig. 3. The micrograph images offered a comprehensive microstructural examination of the particle size, shape, and aggregation of the synthesized materials, and Fig. 3 (a)–(d) show densely packed nonuniform grains with large agglomerations of pure NFO NPs. The larger agglomerations with larger grain sizes enhanced the magnetic moments, and were related to their volume and agglomeration. Furthermore, because of their large agglomerations, the NFO material was permanently magnetized, the average grain size of the NPs ranged between 220 and 250 nm, and homogeneous grains were observed with RE Eu^{3+} oxide [26,35]. Thus, microstructural analysis was essential for comprehending the magnetic enhancement and had a direct impact on the electrical characteristics of the prepared NPs. Large grain sizes may alter the grain (Gs) and grain boundaries (GBs), thus consequently hindering the electric flow in MFe_2O_4 materials. Additionally, micrographs for each of the prepared samples demonstrate the development of cubic grains, essentially indicating that the grains managed to maintain their cubic shape during grain growth [36]. Furthermore, the EDAX measurements suggest that the synthesized Eu-doped NFO was stoichiometric and had a uniform distribution of elements because the average particle size slightly increased with the addition of Eu^{3+} at the Fe^{3+} site, is shown in Fig. 4 (a,b). The percentage of element present and the particle size are givenn in Table 2.

The isothermal magnetic measurements [M(T)] obtained for pure and Eu^{3+} doped NFO NPs in the ZFC and FC modes with an externally μ_0. H of 0.5 T are shown in Fig. 5. Fig. 5 illustrates the difference between the ZFC curve's estimated magnetization of 6.13 emu.g^{-1} at 5 K and the FC curve's increasing magnetization value with decreasing temperature reaching 7.38 emu.g^{-1} at 5 K. The disconnection of the ZFC and FC curves with decreasing temperature indicates the presence of a nonequilibrium magnetization state below 300 K for pure and doped materials, denoted as the T_{irr} (irreversibility temperature), at which the FC and ZFC curves diverge [9,10]. Furthermore, the FC curves revealed that increasing the temperature and decreasing the magnetization between 5 and 300 K resulted in strong dipolar magnetostatic interactions between the individual μ_B for the entire composition. By contrast, the ZFC curves were strongly associated with the energy barrier distribution and high thermal T_{irr}. Furthermore, the Eu^{3+} doped NFO NPs exhibited the same trend as the pure material in that the magnetization value decreased as Eu^{3+} was added to the Fe^{3+} site. According to the differences in the magnetization values in the FC (at 5 K) and ZFC (at 300 K) curves, the tetravalent nonmagnetic REE ions of Eu^{3+} attempted to partially replace the Fe^{3+} ions in the B-sites, which resulted in a net magnetization decrease because the substitution of Eu^{3+} has a lower μ_B (3.5 lB) than that of Fe^{3+} (5 lB), as listed in Table 3. Here, magnetization decreased owing to the μ_B of the REE (Eu^{3+}) ions, which is typically accompanied by localized 4f-electrons. This is because the spins require more thermal energy to be released from the axis of the NPs, thus allowing for the alignment of μ_B with μ_0.H, as the temperature is increased. Most of the saturation magnetization in MFe_2O_4 originates from the interactions between the cations in the A and B sites. Neel's model of FI states that intra-sublattice A–A and B–B interactions are less important than A–B exchange interactions and the net magnetic moment arising from the difference between B of A and B sublattices, as the

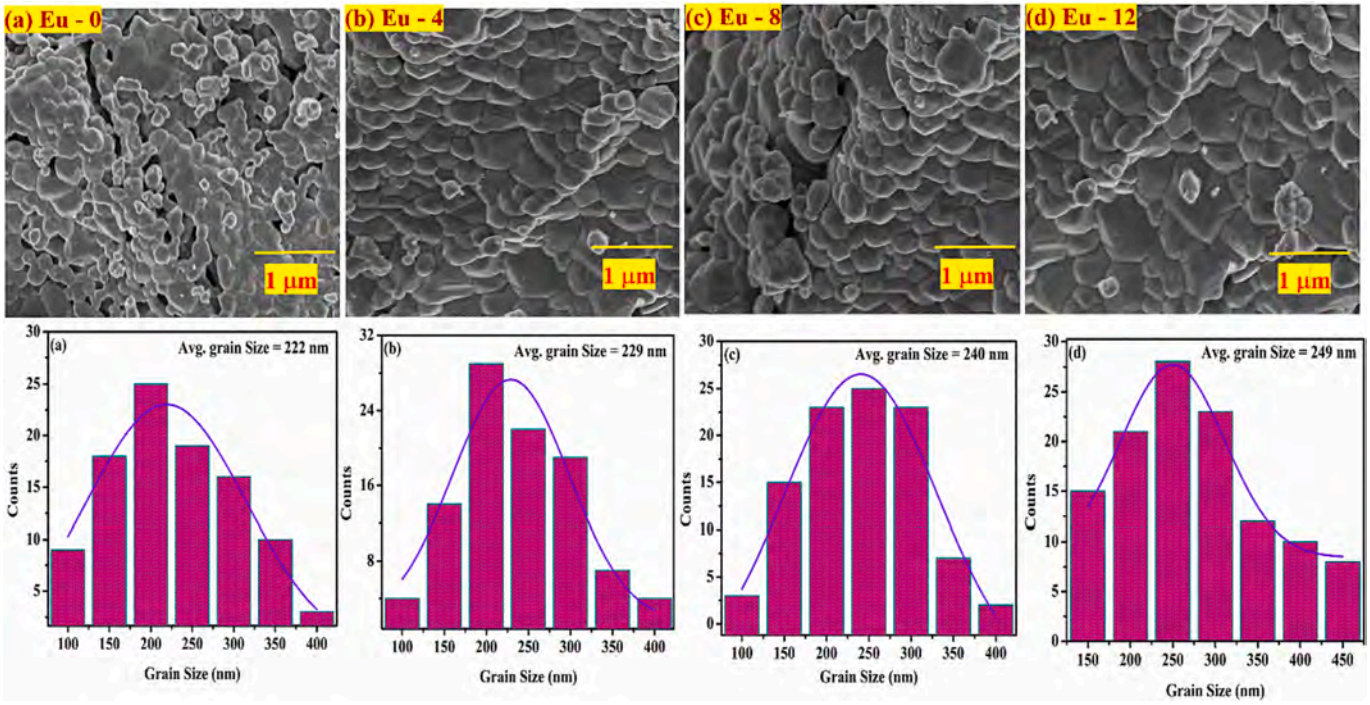

Fig. 3. FESEM of Eu doped NFO NPs; (a) Eu = 0, (b) Eu = 4, (c) Eu = 8 and (d) Eu = 12.

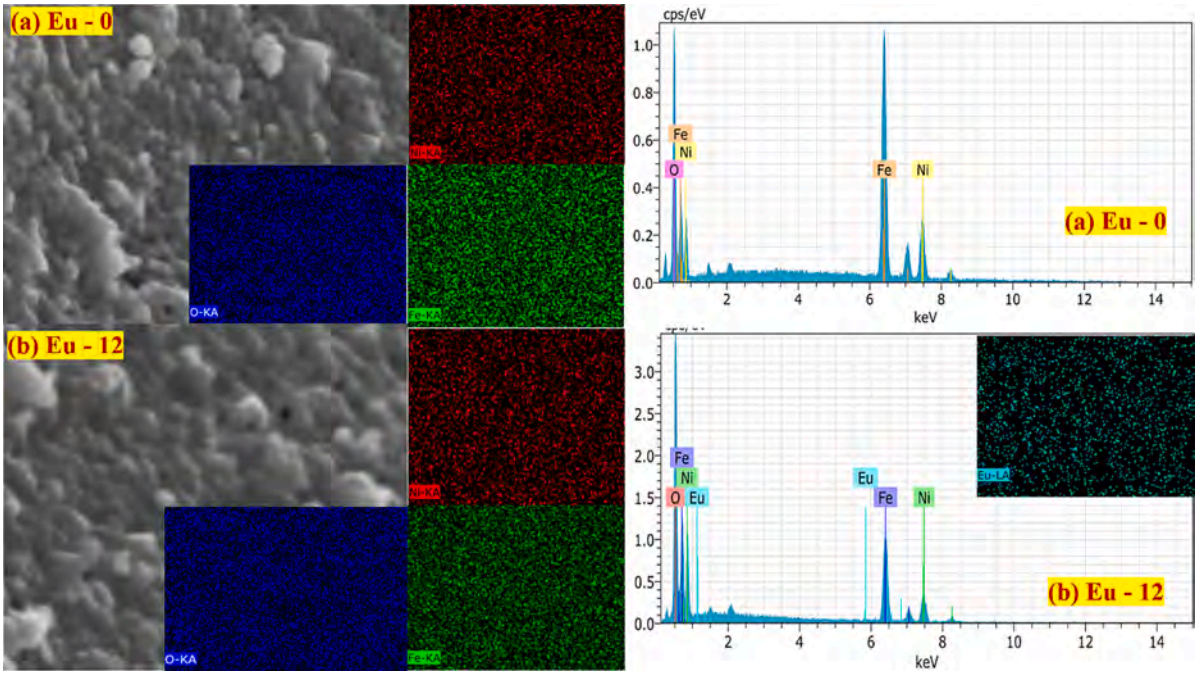

Fig. 4. EDAX and mapping of (a) Pure and (b) Eu = 12 NPs.

Table 2
EDAX analysis and particle size of $NiFe_{2-x}Eu_xO_4$.

x (Eu^{3+})	Ni at. %	Fe at. %	Eu at. %	O at. %	Particle Size (nm)
Eu – 0	19.85	37.36	–	42.79	220
Eu – 4	17.49	36.73	1.98	43.78	229
Eu – 8	18.69	38.76	2.43	40.12	240
Eu – 12	23.43	38.12	4.81	33.64	249

moments of the A and B sublattices are in opposite directions [26]. In MFe_2O_4 materials, Fe^{3+} ions contribute to the magnetization of both the A and B sublattices, whereas Ni^{2+} and Eu^{3+} ions exclusively contribute to the magnetization of the B sublattice. In light of the aforementioned statement, the net μ_B is expected to decrease because of the preferential tenancy of Eu^{3+} ions toward B sites in the NFO spinel lattice to minimize Fe^{3+} ions. The results show that as the concentration of REE Eu^{3+} increases, the net magnetization decreases, which implies that the Fe $(A)^{3+}$–O^{2-}–$Eu(B)^{3+}$ super-exchange interactions are relatively weaker than the $Fe(A)^{3+}$–O^{2-}—$Fe(B)^{3+}$ interactions [32].

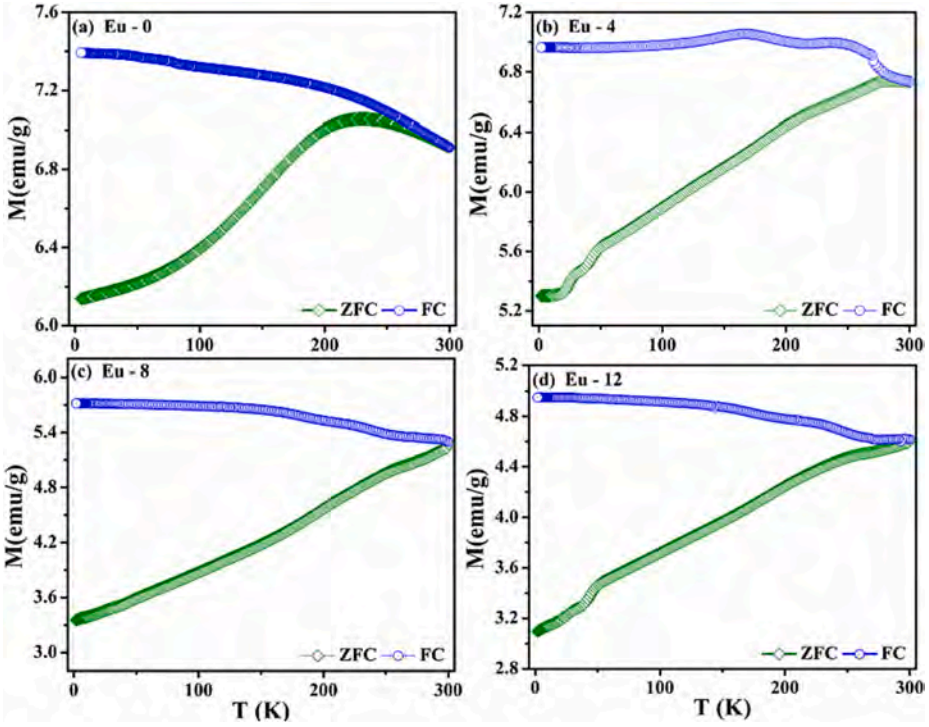

Fig. 5. M(T) of Pure and Eu doped NFO NPs (a) Eu = 0, (b) Eu = 4, (c) Eu = 8 and (d) Eu = 12 at μ_0.H = 0.5 T.

Table 3
The M_S value at 5 K and 300 K from ZFC and FC curve.

Temp K	Eu − 0		Eu − 4		Eu − 8		Eu − 12	
	FC emu. g^{-1}	FC emu. g^{-1}	FC emu. g^{-1}	ZFC emu. g^{-1}	FC emu. g^{-1}	ZFC emu. g^{-1}	FC emu. g^{-1}	ZFC emu. g^{-1}
5 K	7.39	6.13	6.96	5.29	5.71	3.39	4.94	3.10
300 K	6.91	6.91	6.73	6.70	5.28	5.28	4.62	4.62

Fig. 6 shows the isothermal magnetization [M(H)] of Eu^{3+}-doped NFO samples subjected to a magnetic field of 2 T at RT. Evidently, the magnitude of magnetization saturated around 0.5 T for all compositions and remained constant up to the maximum field of 2 T. The M_S value was reduced by the doping of Eu^{3+} at the Fe^{3+} site, and the M_S values for the pure and doped compositions were 48.42, 47.72, 45.27, and 43.15 emu. g^{-1} for Eu = 0, 4, 8, and 12, respectively. The magnified version of Fig. 6 (b) demonstrates that the decrease in Ms and increase in Eu^{3+} resulted from the changes that occurred at the spinel ferrite lattice sites as the REE oxide content increased. Similarly, doping with REE Nd^{3+} and Eu^{3+} oxide elements resulted in decreasing trends in the M_S values [26,36,37]. In general, the ability of metal cations to occupy B and A sites varies depending on the ionic radii of the selected elements, and trivalent Fe^{3+} ions in the spinel lattice were replaced with higher ionic radii Eu^{3+} ions, thus influencing the magnetic exchange interactions and leading to changes in the magnetic properties of the preferred composition. The magnetization of MFe_2O_4 NPs is generally determined by changes in the crystallite size, μ_B, and the occupancy site of the cation [35]. In addition, the magnetic behavior of MFe_2O_4 NPs is influenced by disordered metal cations and super exchange interactions, as well as by the composition of Eu^{3+}-doped NFO. Further, trivalent Fe^{3+} ions, an important component in MFe_2O_4, typically form magnetic moments. Consequently, dopants may be able to replace Fe^{3+} ions (Eu^{3+}–O–Fe^{3+}) via 4f–3d couplings to affect the magnetic exchange interactions between Fe^{3+}–O–Fe^{3+} ions and incorporation of Eu^{3+} ions in the NFO spinel lattice. Therefore, the ionic radii of the elements play a significant role, and the A–B interactions between the REE oxides and MFe_2O_4 lattice increase or decrease the magnetic properties of the prepared NPs. MFe_2O_4 NPs decreasing magnetization trend was attributed to replacing Fe^{3+} (0.64 Å) ions on the B sites with larger ionic radii Eu^{3+} (1.01 Å) ions, which was preferable for the A sites to be occupied by smaller ionic radii ions. The M(T) curve reveals the soft FM nature at both low and high temperatures, as confirmed from the M(H) curve for the pure and Eu-doped samples shown in the zoomed view of Fig. 6 (b) and (c). Subsequently, M(H) measurements of Eu^{3+}-doped NFO were performed at lower and higher temperatures of 10, 100, 200, and 300 K in μ_0. H = 2.5 T is shown in Fig. 7. The M_S value increased for every composition as the temperature decreased, as represented by the M(T) FC curve. The M_S value of pure and doped compositions were 53.71, 51.82, and 49.15 emu.g^{-1} [at 10 K] for Eu = 0, 8, and 12, respectively. The presence of a soft FM hysteresis loop at both lower and higher temperatures indicates that Eu doping at the Fe site confirms its soft FM nature.

The magnetic properties of Ms, H_C, Mr (magnetic remanence), and squareness ratio (Rs) values are listed in Table 4. The Mr values of the Eu-doped NPs ranged from 32.64 to 23.65 emu.g^{-1} and M_r values decreased as the number of substituted elements (Eu^{3+}) in NFO increased. The same behavior has been observed in Dy^{3+}-doped NFO and Gd^{3+} doped CFO [37,38]. Additionally, the same pattern in M_r values was observed in the M_S of the prepared NPs, thus indicating that M_r was dependent on both the M_S of the synthesized NPs and the grain alignment induced by the super-exchange interactions among the MFe_2O_4 NPs. Furthermore, the H_C of the material was a significant factor in the magnetic properties of the MFe_2O_4 NPs, and the values of H_C for the Eu-doped samples were 96, 118, 126, and 140 Oe for Eu = 0, 4, 8, and 12, respectively. The H_C increased with the concentration of Eu^{3+}, which may be a result of the enhancement of magnetocrystalline anisotropy with anisotropic Fe^{2+} ions situated at tetrahedral sites [39]. Additionally, H_C is considered to be a microstructural property and is influenced by a variety of elements, including the material's surface effect, strains, nonmagnetic atoms, magnetic exchange interactions between collinear spins and canted spins over the core, and material defects [40,41]. Furthermore, the parameter Rs was derived from the ratio of M_r/M_S, and these values decreased as Eu increased at the Fe site. A

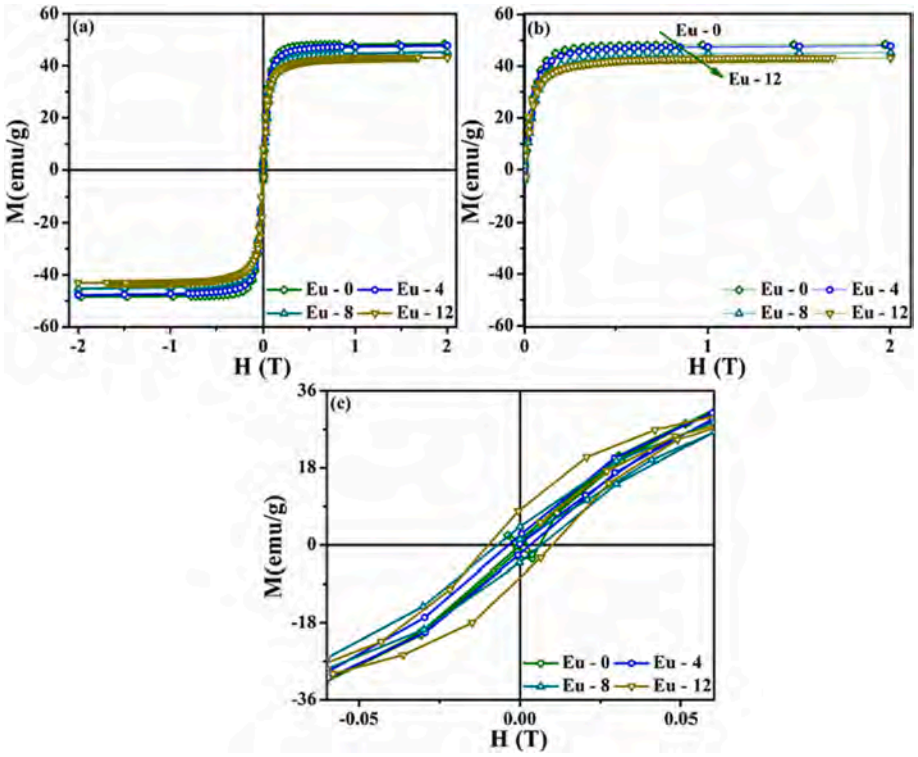

Fig. 6. Isothermal curve of Eu doped NFO NPs (a) full view and (b-c) Zoomed view at μ_0.H = 2.0 T.

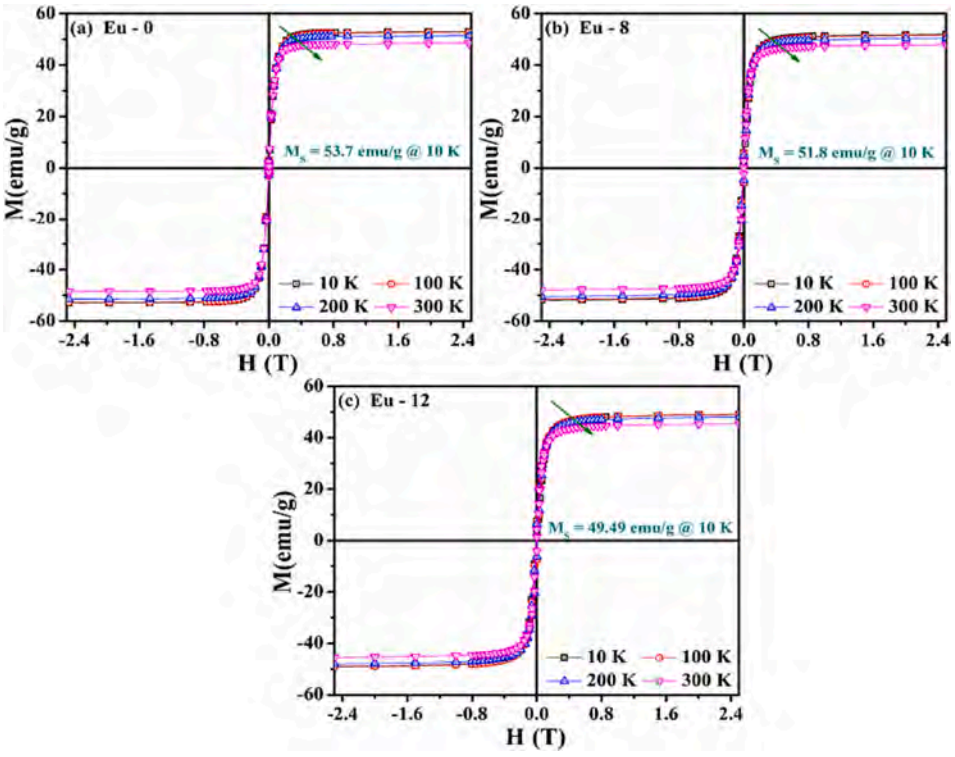

Fig. 7. Isothermal curve of Eu doped NFO NPs (a) Eu = 0, (b) Eu = 8, (c) Eu = 12 at lower and ambient temperature.

high value of Rs is generally preferred for the application of memory devices and recording media. Moreover, the presence of magnetostatic interactions in multi-domain NPs at RT is demonstrated by the Rs being greater than 0.5 for all compositions, and a higher Rs is indicative of a random orientation, similar to that of noninteracting NPs with cubic magnetocrystalline anisotropy [42–44]. Fig. 8 shows a graphic representation of M_r, M_S, and Rs of the Eu-doped NFO NPs at RT. In general, the reduction in remanent magnetization (Mr) is faster than the reduction in saturation magnetization (Ms) is commonly observed in magnetic materials and is often associated with factors such as magnetic domain

Table 4
Magnetic parameters for Eu^{3+} doped $NiFe_2O_4$ at 300 K. Fig. 1:

Eu^{3+}	Ms	M_r	Hc	Rs
Eu – 0	48.42	32.64	96	0.674
Eu – 4	47.72	29.97	118	0.628
Eu – 8	45.27	26.79	126	0.591
Eu – 12	43.15	23.65	140	0.548

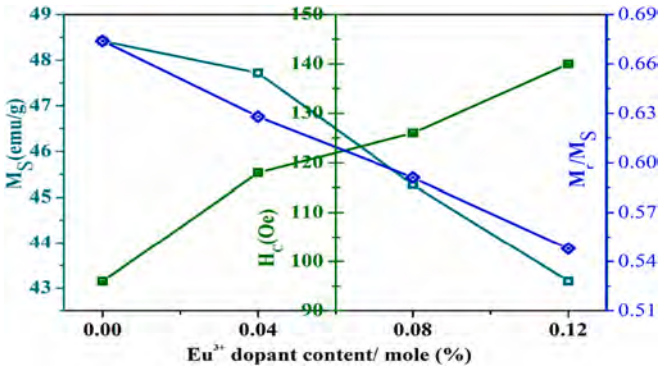

Fig. 8. Graphical representation of M_S, H_C, and Rs of Eu doped NFO NPs.

behavior, defects, and microstructural changes in the materials.

The room temperature permittivity (ε'), imaginary part (ε') of the dielectric, and loss factor (tan δ) for frequencies ranging from 100 Hz to 2 MHz reveal that a common behavior occurred and the ε' value decreased for the entire sample with an increase in frequency between 1 kHz and 2 MHz, thus indicating the dielectric's normal dispersion behavior, as shown in Fig. 9 (a). In general, ferrite materials are made up of strongly conducting grains (Gs) and poorly conducting grain boundaries (GBs). Space charge polarization occurs when electrons accumulate at the poorly conducting GBs, as a result, the value of ε′ is high at lower frequencies. The dielectric dispersion suggests the real dielectric constant varies significantly with frequency, which is supported by the Koop's theory. According to Koop's theory, the materials can be composed of two layers [10,45,46]. The first consists of highly conducting large layers of Gs (grains) separated by short and low conducting layers of GBs (grain boundaries). GB effects are dominant at lower frequencies, whereas Gs are effective at higher frequencies. According to Koop's theory, the dielectric structure has well-dielectric Gs with poorly separated GBs, and Maxwell–Wagner interfacial polarization, which is in good agreement with Koop's theory, leads to the observation of a higher value or dispersion of ε' for the ferities at lower frequencies. Based on this theory, dispersion is influenced by the inhomogeneous nature of the dielectric structure, which is intended to consist of two layers. The combined responses from the ionic, space charge, and interface polarizations are responsible for the observation of the maximum dielectric constant value in the lower frequency region, and interfacial polarization occurs when different conductivity phases coexist in the same material. The observation of an independent ε' in the higher-frequency region implies that the dipole cannot be maintained with variations caused by changes in the applied electric field. Thus, the analysis suggests that the Gs are effective at higher frequency regions, whereas GBs are more effective for ε' at lower frequency regions. The electron exchange between Fe^{2+} and Fe^{3+} ions is independent of the frequency of the applied AC electric field in MFe_2O_4, where the polarization in NFO is related to charge carrier hopping [47]. This may be because an increase in the frequency of the applied AC electric field caused the polarization to decrease. Hence, the analysis reveals that with the addition of Eu^{3+} at the Fe^{3+} site, the material's ε' decreased whereas the amount of nonmagnetic ions increased, and the doping of Eu^{3+} ions did not have a greater impact on the higher frequency region. Hence, when Eu^{3+} was added to the Fe^{3+} site, the increase in Eu^{3+} concentration changed some Fe^{3+} ions to Fe^{2+} to create charge neutrality, which may also be responsible for the decreased hopping between Fe^{3+} and Fe^{2+} ions and decrease in grain resistance, all of which contributed to the decrease in ε' of the material. The ε" is plotted against frequencies at different temperatures in Fig. 9 (b). In the case of ε', a similar pattern was obtained for ε" [48,49]. This is because polarization in a dielectric material is predominantly driven by dipole alignment, which is related to charge carrier movement in response to an electric field. Nonmagnetic Eu^{3+} ions have the ability to cause dipole alignment problems and impede polarization generation, which reduces the material's total polarization.

The ratio of ε" to ε' of the dielectric constant can be used to express tan, δ which is generally used to describe energy losses, and here, δ (angle). According to Fig. 9 (c), the loss tangent had very low values across the entire temperature and frequency range, thus indicating an inherent property of the material. Typically, tan δ is attributed to the dipole polarization lag that occurs after the applied alternating field and might be caused by crystal lattice imperfections, GBs, and impurities of MFe_2O_4 [45]. Additionally, the frequency-dependent dispersion of tan δ, which also begins decreasing with the substitution of Eu^{3+}, can be explained by the Maxwell–Wagner model. Thus, the density of the materials plays a critical role in controlling the loss variations. As the presence of Gs in the low-frequency region typically corresponds to a high resistivity (reason GB) and vice versa, and because of the high energy needed for electron exchange between Fe^{2+} and Fe^{3+} ions in the low-frequency region, a loss in the material occurs [50,51]. Similarly, when the frequency is high, less energy is required for electron transfer between the two Fe ions at the B site, and at higher frequencies, the value of ε″ decreases, thus indicating its suitability for use in high-frequency devices.

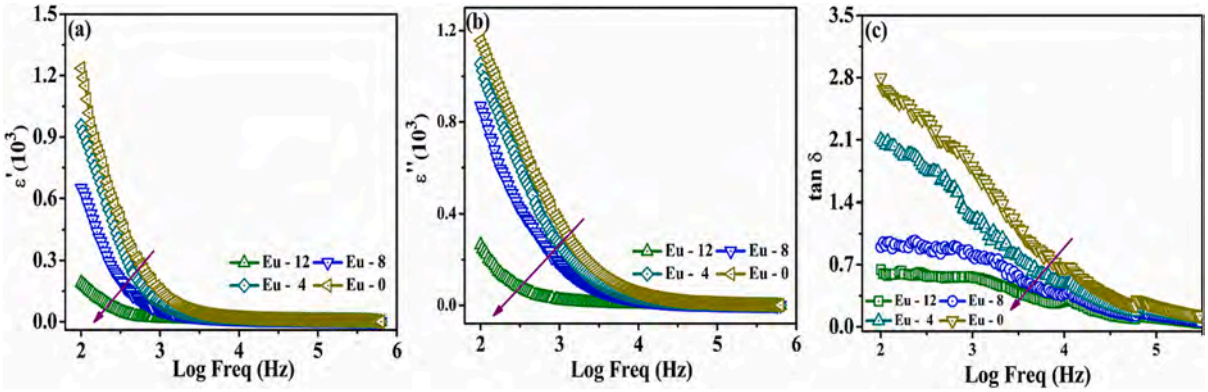

Fig. 9. (a) ε', (b) ε" and (c) tan δ of Eu doped NFO NPs.

4. Conclusion

Herein, the physical, electrical, and magnetic characteristics of Eu^{3+}-doped NFO materials were analyzed using PXRD, FESEM, EDAX, and MPMS techniques. The PXRD analysis confirmed the lower Eu^{3+} substitutions ($Eu^{3+} = 4$ and 8) and secondary phases of $EuFe_2O_3$ for higher substitution ($Eu^{3+} = 12$), and the change in ac revealed that the spinel lattice sites are responsible for the vacancies in MFe_2O_4. In addition, the higher ionic radii of Eu at sites with lower ionic radii of Fe seem to be due to changes in ac and crystalline size. The formation of nano-crystalline grains with a spherical morphology was revealed by micro-structural features, and the EDAX spectrum showed no evidence of contamination. The particle size obtained from the microstructural analysis increased with increasing ac because of the higher ionic radii of Eu^{3+}. Further. Magnetic studies at both RT and lower temperatures unquestionably demonstrate that soft FM behavior and Ms and Mr values increased with increasing Eu concentration at RT, and that the decrease in RT magnetization resulted from large lattice distortions caused by Eu^{3+} ions and cation distribution at different sites. The decrease in ε' and tan δ was caused by the reduced hopping rate that resulted from the substitution of Eu^{3+} ions for Fe^{3+} ions at the B sites. Thus, REE-doped ferrite NFO materials are extremely beneficial for a variety of applications in microwave devices and aerospace applications.

Declaration of competing interest

The authors declare that they have no known competing financial interests or personal relationships that could have appeared to influence the work reported in this paper.

Data availability

Data will be made available on request.

Acknowledgements

The research was supported by the National Research Foundation of Korea (NRF) grant funded by the Korea government (MIST) (No. 2022R1C1C1006414). Also, this research was supported by Korea Basic Science Institute (National research Facilities and Equipment Center) grant funded by the Ministry of Education (2019R1A6C1010046).

Data and code availability:

Data will be made available on request

Ethical Approval:

Not applicable

References

[1] R.H. Kadam, S.T. Alone, M.L. Mane, A.R. Biradar, S.E. Shirsath, Phase evaluation of Li+ substituted CoFe2O4 nanoparticles, their characterizations and magnetic properties, J. Magn. Magn. Mater. 355 (2014) 70.

[2] D.M. Jnaneshwara, D.N. Avadhani, B.D. Prasad, B.M. Nagabhushana, H. Nagabhushana, S.C. Sharma, C. Shivakumara, J.L. Rao, N.O. Gopal, S.C. Ke, R.P. S. Chakradhar, Electron paramagnetic resonance, magnetic and electrical properties of CoFe2O4 nanoparticles, J. Magn. Magn. Mater. 339 (2013) 40.

[3] K. Sasikumar, R. Bharathikannan, G. Sujithkumar, S. Raja, G. Johnsy Arputhavalli, M. Vidhya, R. Marnadu, R. Suresh, Structural, Optical, and Magnetic Properties of Mn-Doped Nickel Ferrite (Ni1-xMnxFe2O4) Thin Films Deposited by Jet Nebulizer Spray Pyrolysis Technique, J. Supercond. Nov. Magn. 34 (2021) 2189–2198.

[4] O.h. Yumi, Manisha Sahu, Sugato Hajra, Aneeta Manjari Padhan, Swati Panda, Hoe Joon Kim, Spinel Ferrites (CoFe2O4): Synthesis, Magnetic Properties, and Electromagnetic Generator for Vibration Energy Harvesting, J. Electron. Mater. 51 (2022) 1933.

[5] O.h. Wonjeong, Sugato Hajra, S Divya, Swati Panda, Yumi Oh, Zvonko Jaglic, Phakkhananan Pakawanit, Tae Hwan Oh, Hoe Joon Kim, Contact electrification of porous PDMS-nickel ferrite composites for effective energy harvesting, Mater. Sci. Eng. B 292 (2023) 116397.

[6] A. Sivakumar, S Sahaya Jude Dhas, P Sivaprakash, Abdulrahman I Almansour, Raju Suresh Kumar, Natarajan Arumugam, Karthikeyan Perumal, S Arumugam, SA Martin Britto Dhas, Raman Spectroscopic and Electrochemical Measurements of Dynamic Shocked MnFe2O4 Nano-crystalline Materials, J Inorg Organomet Polym Mater. 32 (2022) 344–352.

[7] L.T. Lu, N.T. Dung, L.D. Tung, C.T. Thanh, O.K. Quy, N.V. Chuc, S. Maenosono, N. T. Thanh, Synthesis of magnetic cobalt ferrite nanoparticles with controlled morphology, monodispersity and composition: the influence of solvent, surfactant, reductant and synthetic conditions, Nanoscale. 46 (2015) 19596.

[8] D. Carta, M.F. Casula, A. Falqui, D. Loche, G. Mountjoy, C. Sangregorio, A. Corrias, A Structural and Magnetic Investigation of the Inversion Degree in Ferrite Nanocrystals MFe2O4 (M = Mn Co, Ni), J. Phys. Chem. c. 113 (2009) 8606–8615.

[9] P. Sivaprakash, S. Divya, R. Parameshwari, C. Saravanan, S. Suresh Sagadevan, S. E. Arumugam, Muthu, Influence of Zn2+ doping towards the structural, magnetic, and dielectric properties of NiFe2O4 composite, J. Mater. Sci.: Mater. Electron. 31 (2020) 16369.

[10] S. Divya, P. Sivaprakash, S. Raja, S. Esakki Muthu, E.M. Eed, S. Arumugam, Tae Hwan Oh, Temperature-dependent dielectric and magnetic properties of NiFe2O4 nanoparticles, Appl Nanosci 13 (2023) 1327–1336.

[11] S. Divya, J. Hemalatha, Structural and electrical properties of P(VDF-HFP)/ ZnFe2O4, nanocomposites, Ferroelectrics 519 (2017) 152–156.

[12] A. Ramakrishna, N. Murali, S.J. Margarette, T.W. Mammo, N.K. Joythi, B. Sailaja, C.C. Sailaja-Kumari, K. Samatha, V. Veeraiah, Studies on structural, magnetic, and DC electrical resistivity properties of Co0.5M0.37Cu0.13Fe2O4 (M = Ni, Zn and Mg) ferrite nanoparticle systems, Adv Powder Tech 29 (2018) 2601–2607.

[13] S.E. Shirsath, D. Wang, S.S. Jadhav, M.L. Mane, S. Li, Ferrites obtained by sol–gel method. Handb Sol-Gel, Sci Technol (2018), https://doi.org/10.1007/978-3-319-19454-7_125-3.

[14] S. Divya, P. Sivaprakash, S. Raja, S. Esakki Muthu, N. Ikhyun Kim, S.A. Renuka, Tae Hwan Oh, Impact of Zn doping on the dielectric and magnetic properties of CoFe2O4 nanoparticles, Ceram. Int. 48 (2022) 33208.

[15] N. Rezlescu, E. Rezlescu, The Influence of Fe substitutions by R ions in a Ni-Zn ferrite, Solid State Commun. 88 (1993) 139.

[16] K. Kamala Bharathi, K. Balamurugan, P. Santhosh, M. Pattabiraman, G. Markandeyulu, Magnetocapacitance in Dy-doped Ni ferrite, Phys Rev b. 77 (2008) 172401.

[17] E. Schloemann, Advances in ferrite microwave materials and devices, J. Magn. Magn. Mater. 209 (2000) 15.

[18] E. Ateia, M.A. Ahmed, A.K. El-Aziz, Effect of rare earth radius and concentration on the structural and transport properties of doped Mn-Zn ferrite, J. Magn. Magn. Mater. 311 (2007) 545.

[19] J. Song, L.X. Wang, N.C. Xu, Q.T. Zhang, Microwave electromagnetic and absorbing properties of Dy3+ doped MnZn ferrites, J Rare Earths. 28 (2010) 451.

[20] B.F. Ji, C.A. Tian, Q.Z. Zhang, D.D. Ji, J. Yang, J.S. Xie, et al., Magnetic properties of samarium and gadolinium co-doping Mn-Zn ferrites obtained by sol-gel auto combustion method, J Rare Earths. 34 (2016) 1017.

[21] Y. Mohammadifar, H. Shokrollahi, Z. Karimi, L. Karimi, The synthesis of Co1−xDyxFex-2O4 nanoparticles and thin films as well as investigating their magnetic and magneto-optical properties, J. Magn. Magn. Mater 366 (2014) 44–49.

[22] F. Jin, Y.M. Zhu, L. Li, Z.Z. Pan, D.S. Pan, M. Gu, Q. Li, L. Chen, H. Wang, Robust ferrimagnetism and switchable magnetic anisotropy in high-entropy ferrite film, Adv. Funct. Mater. 2214273 (2023).

[23] S. Mahalakshmi, K. SrinivasaManja, S. Nithiyanantham, Electrical properties of nanophase ferrites doped with rare earth ions, J. Supercond. Nov. Magn 27 (2014) 2083–2088.

[24] M.A. Almessierea, Y. Slimani, S. Güner, M. Nawaz, A. Baykal, F. Aldakheel, S. Akhtar, I. Ercan, İ. Belenli, B. Ozçelik, Magnetic and structural characterization of Nb3+-substituted CoFe2O4 nanoparticles, Ceram. Int. 45 (2019) 8222 – 8232.

[25] M.A. Almessiere, Y. Slimani, S. Güner, A. Baykal, I. Ercan, Effect of dysprosium substitution on magnetic and structural properties of NiFe2O4nanoparticles, J. Rare Earths 37 (2019) 871–878.

[26] A. Zubair, A. Mahmood, W.-C. Cheong, I. Ali, Muhammad Azhar Khan, Adeel Hussain Chughtai, Zahoor Ahmad, Muhammad Naeem Ashiq, Structural, morphological and magnetic properties of Eu-doped CoFe2O4 nanoferrites, Results Phys. 7 (2017) 3203–3208.

[27] K. Elayakumar, A. Dinesh, A. Manikandan, G. Murugesan Palanivelu, S. Kavitha, R. T. Prakash, S.K. Kumar, A.B. Jaganathan, Structural, Morphological, Enhanced Magnetic Properties and Antibacterial Biomedical Activity of Rare Earth Element 476 (2019) 157–165. REE) Cerium (Ce3+) doped CoFe2O4 nanoparticles.

[28] S. Ravi Kumar, G. Vishnu Priya, B. Aruna, M.K. Raju, D. Parajuli, N. Murali, R. Verma, K.M. Batoo, P.V. Rajesh Kumar, L. Narayana, Influence of Nd3+ substituted Co0.5Ni0.5Fe2O4 ferrite on structural, morphological, dc electrical resistivity and magnetic properties, Inorg. Chem. Commun. 136 (2022) 109132.

[29] M.N. Akhtar, M. Yousaf, L.u. Yuzheng, M.Z. Mahmoud, J. Iqbal, M.A. Khan, M. U. Khallidoon, S. Ullah, M. Hussien, Magnetic, structural, optical band alignment and conductive analysis of graphene-based REs (Yb, Gd, and Sm) doped NiFe2O4 nanocomposites for emerging technological applications, Synth. Met. 284 (2022) 116994.

[30] W.S. Mohamed, A.M. Abu-Dief, Impact of rare earth europium (RE-Eu3+) ions substitution on microstructural, optical and magnetic properties of CoFe2−xEuxO4 nanosystems, Ceram. Int. 46 (2020) 16196–16209.

[31] R. Sankaranarayanan, S. Shailajha, M.S. Kairon Mubina, C.P. Anilkumar, Influence of divalent ions on structural, magnetic and electrical response of CozCdyZnxNi(1-x-y-z) Fe2O4 core materials, J. Magn. Magn. Mater 529 (2021) 167892.

[32] Mritunjoy Prasad Ghosh, Saurabh Sharma, Harendra Kumar Satyapal, Kamar Tanbir, Rakesh Kumar Singh, Samrat Mukherjee, Tuning the microstructural, optical and superexchange interactions with rare earth Eu doping in nickel ferrite nanoparticles, Mater. Chem. Phys. 241 (2020) 122383.

[33] S. Hassan, M. Ahmad, A. ur Rehman, M.W. Iqbal, S.F. Shaukat, H.S. Abd-Rabboh, Structural, magnetic and electrochemical properties of Al-substituted Ni ferrites for energy storage devices, J. Energy Storage 55 (2022) 105320.
[34] Majid Niaz Akhtar, Muhammad Shahid Nazir, Muhammad Azhar Khan, Sami Ullah, Mohammed Ali Assiri, Preparations and characterizations of Ca doped Ni–Mg–Mn nanocrystalline ferrites for switching field high-frequency applications, Ceram. Int. 48 (2022) 3833.
[35] Y. Slimani, M.A. Almessiere, M. Nawaz, A. Baykal, S. Akhtar, I. Ercan, I. Belenli, Effect of bimetallic (Ca, Mg) substitution on magneto-optical properties of NiFe2O4 nanoparticles, Ceram. Int. 45 (2019) 6021–6029.
[36] K.L. Routray, D. Behera, Enhancement in conductivity and dielectric properties of rare-earth (Gd3+) substituted nano-sized CoFe2O4, J. Mater. Sci.: Mater. Electron. 29 (2018) 14248–14260.
[37] Yuzheng Lu, Muhammad Yousaf, Majid Niaz Akhtar, Asma Noor, Muhammad Akbar, M.A.K. Yousaf Shah, Senlin Yan, Faze Wang, Effect of Gd and Co contents on the microstructural, magneto-optical and electrical characteristics of cobalt ferrite (CoFe2O4) nanoparticles, Ceram. Int. 48 (2022) 2782 – 2792.
[38] A. Anwar, S. Zulfiqar, M.A. Yousuf, S.A. Ragab, Muhammad Azhar Khand, Imran Shakir, Muhammad Farooq Warsi, Impact of rare earth Dy+3 cations on the various parameters of nanocrystalline nickel spinel ferrite, J. Mater. Res. Technol. 9 (2020) 5313.
[39] F. Aen, S.B. Niazi, M.U. Islam, M.U. Mukhtar Ahmad, Rana, Effect of holmium on the magnetic and electrical properties of barium-based W-type hexagonal ferrites, Ceram. Int. 37 (2011) 1725–1729.
[40] P.K. Roy, B.B. Nayak, J. Bera, Study on electro-magnetic properties of La substituted Ni–Cu–Zn ferrite synthesized by auto-combustion method, J. Magn. Magn. Mater 320 (2008) 1128–1132.
[41] S.E. Shirsath, R.H. Kadam, A.S. Gaikwad, A. Ghasemi, Akimitsu Morisako, Effect of sintering temperature and the particle size on the structural and magnetic properties of nanocrystalline Li0.5Fe2.5O4, J. Magn. Magn. Mater 323 (2011) 3104–3108.
[42] S.I. El-Dek, Effect of annealing temperature on the magnetic properties of CoFe2O4 nanoparticles, Philos. Mag. Lett. 90 (2010) 233–240.
[43] J. Sahadevan, M. Radhakrishnan, N. Padmanathan, S. Esakki Muthu, P. Sivaprakash, M. Kadiresan, Effect of Mn substitution on magnetic behaviour of oxygen defective LaCoO3 perovskite oxide, Mater Sci Eng B 284 (2022) 115875.
[44] P. Jhelai Sahadevan, S.E. Sivaprakash, I.K. Muthu, N. Padmanathan, V. Eswaramoorthi, Influence of Te-Incorporated LaCoO3 on Structural, Morphology and Magnetic Properties for Multifunctional Device Applications, Int. J. Mol. Sci. 24 (2023) 10107.
[45] M.A. Ahmed, N. Okasha, R.M. Kershi, Extraordinary role of rare-earth elements on the transport properties of barium W-type hexaferrite, Mater. Chem. Phys 113 (2009) 196–201.
[46] M. Atif, M.W. Asghar, M. Nadeem, W. Khalid, Z. Ali, S. Badshah, Synthesis and investigation of structural, magnetic and dielectric properties of zinc substituted cobalt ferrites, J. Phys. Chem. Solid. 123 (2018) 36–42.
[47] U.R. Ghodake, N.D. Chaudhari, R.C. Kambale, J.Y. Patil, S.S. Suryavanshi, Effect of Mn2+ substitution on structural, magnetic, electric and dielectric properties of Mg Zn ferrites, J. Magn. Magn. Mater. 407 (2016) 60–68.
[48] P. Sivaprakash, A.N. Ananth, V. Nagarajan, S.P. Jose, S. Arumugam, Remarkable enhancement of La(1–x)SmxCrO3 nanoperovskite properties: an influence of its doping concentrations, Mater. Res. Bull. 95 (2017) 17–22.
[49] S. Arumugam, P. Sivaprakash, A. Dixit, R. Chaurasiya, L. Govindaraj, M. Sathiskumar, S. Chatterjee, R. Suryanarayanan, Complex magnetic structure and magnetocapacitance response in a non-oxide NiF 2 system, Sci. Rep. 9 (2019) 1–8.
[50] R.V. Mangalaraja, P. Manohar, F.D. Gnanam, Electrical and magnetic properties of Ni0.8Zn0.2Fe2O4/silica composite prepared by sol-gel method, J. Mater. Sci. 39 (2004) 2037.
[51] P. Sivaprakash, A. Nitthin Ananth, V. Nagarajan, R. Parameshwari, S. Arumugam, P. Sujin, S. Jose, Esakki Muthu, Role of Sm3þ dopant in the formation of La(1–x) SmxCrO3 solid state nano perovskites – Correlation of its augmented physical properties, Mater. Chem. Phys 248 (2020) 122922.